Chapter 10
Local Ordering at the Interface of the TiO_2-WO_3 Bi-Layers

Dan Macovei, Vasile Dăscăleanu, Cristian M. Teodorescu and Dumitru Luca

Abstract Reducing the recombination rate of photo-generated electron-hole pairs in the surface of pristine TiO_2 materials can be done, among others, via local spatial charge separation in the photocatalytically active surface region. A local electric field acting for this purpose can be ensured, for instance, in hetero-junction regions formed at the interface between a TiO_2 film and a WO_3 ultra-thin layer. The option for the WO_3–TiO_2 semiconductor pair is related to the suitable fit of their band structures. To model the interface, a more in-depth knowledge of local atomic environment is required. Here, we discuss the local atomic ordering and the related effects in the interface region of TiO_2/WO_3 and WO_3/TiO_2 structures grown on Si (100) substrates. Materials characterization was done by using XRD, XPS and XAS techniques. We demonstrate that tungsten atoms enter as W^{6+} or W^{4+} cations into the rutile-type TiO_2 lattice, by substituting the Ti^{4+} cations. While W^{6+}-Ti^{4+} substitution leaves the surrounding rutile matrix unchanged, the W^{4+}-Ti^{4+} substitution induces a local rutile-to-anatase transition. The current results are relevant in designing new applications structures with enhanced photocatalytic performances.

10.1 Introduction

TiO_2 is known as one of the most stable and highly reactive photocatalysts in a wide range of applications, recommended by low cost, non-toxicity, and long-life operation. It is extensively applied to degrade organic pollutants and for air purification, photocatalytic sterilization, reduction of nitrogen to ammonia, water splitting, electrochemical conversion of solar energy [1]. Under UV light irradiation, titania films feature super-hydrophilicity, therefore being used in surface self-cleaning and antifogging applications [1]. Yet, pristine TiO_2 materials'

D. Macovei · C.M. Teodorescu
National Institute of Materials Physics, 077125 Măgurele-Ilfov, Romania

V. Dăscăleanu · D. Luca (✉)
Alexandru Ioan Cuza University, Iasi, Romania
e-mail: dumitru.luca@uaic.ro

I. Tiginyanu et al. (eds.), *Nanostructures and Thin Films for Multifunctional Applications*, NanoScience and Technology,
DOI 10.1007/978-3-319-30198-3_10

applications are associated with two shortcomings: (i) limited photo-activation to only UV range (i.e. less than about 5 % of the sunlight energy), and (ii) limited catalytic activity lifetime, due to due to the recombination of the photo-generated electron-hole pairs on defect centers [2].

TiO_2 photo-activity has been improved by doping with transition metals [3–6], rare earths [7–10] or non-metals [11–16], resulting in extension of the optical response from UV towards the blue region of the visible light. Non-metal dopants are generally considered as more effective, since they lead to both band-gap narrowing and charge-carrier separation, whereas the metal doping often enhances carrier trapping on the localized metal states in the band gap of TiO_2. However, W-doped TiO_2 materials received much attention, due to associated significant improvement of the photocatalytic activity in comparison with pristine TiO_2. The Ti substitution by W^{6+} ions modifies the electronic structure of the TiO_2 host, resulting in a better charge separation and higher photocatalytic efficiency [17]. Besides, the Ti^{4+} substitution by higher-valence cations (like W^{6+}) generates Ti^{3+} ions, in order to maintain the electrical neutrality of the lattice. These ions reduce the carrier recombination rate, thus enhancing the photocatalytic activity. Such a mechanism is similar to that proposed by Yu et al. for F-doped TiO_2 [14] to explain the improved lifetime of the photo-generated carriers and enhanced quantum efficiency.

An alternate way to overcome the TiO_2 shortcomings consists in its coupling with other semiconductors such as CdS, ZnO, SnO_2, SiO_2 or WO_3, featuring different energy levels [18]. In such heterogeneous semiconductor systems, the transfer of the photo-generated carriers between the two semiconductors considerably lowers the recombination rate, thus improving the efficiency of the photocatalytic reactions. Among these hetero-junctions, that between WO_3 (E_g = 2.8 eV) and TiO_2 (E_g = 3.2 eV for anatase and 3.0 eV for rutile) is of particular interest, due to the suitable distribution of the valence and conduction bands. This facilitates charge separation, by transferring the photo-generated electrons from the conduction band of TiO_2 towards WO_3 (with a lower bottom of the conduction band), while the holes move from WO_3 into the valence band of TiO_2 [17].

While the photocatalytic properties of the TiO_2-WO_3 hetero-junctions, as well as their connection with the electronic structure, were widely studied, little attention has been paid to their interface interaction from a structural point of view. We report here on the interface structural interactions in rutile TiO_2-WO_3 photocatalytic bilayer films, prepared by plasma vapor deposition (PVD). The structure and chemical composition of the films were investigated by X-ray diffraction (XRD), X-ray absorption near-edge structure (XANES) spectroscopy, extended X-ray absorption fine-structure (EXAFS) spectroscopy, and X-ray photoelectron spectroscopy (XPS). We show that the oxide layers interact at their interface, with the W diffusion into the TiO_2 lattice, on Ti sites, as W^{6+} and W^{4+} ions. The Ti^{4+} substitution by W^{6+} leaves the surrounding rutile host unchanged, while the substitution by W^{4+} (of larger radius than Ti^{4+}) changes the local environment towards a dilated anatase-like structure.

10.2 Materials and Methods

Bilayer TiO_2/WO_3 (TWS) and WO_3/TiO_2 (WTS) thin films were sequentially deposited on Si(100) substrates, by using an RF magnetron sputtering facility (Hüttinger, PFG 300 RF; 13.56 MHz, 2×10^{-5} mbar base pressure). The details of the preparation were given elsewhere [19]. The deposition setup was equipped with two ceramic disk targets (K. J. Lesker, 99.9 % purity), with a diameter of 76.2 mm. The RF power injected in the discharge (in Ar gas), via an automatic matching box, was adjusted to 70 W to deposit the TiO_2 layers and to 50 W for the WO_3 layers. The deposition pressure (4×10^{-3} mbar) and the target-substrate distance (5 cm) were maintained constant during deposition in all experiments. The film thickness was determined by an in situ quartz microbalance (Sigma Instruments, SQM-160), calibrated against a surface profilometer, prior to deposition experiments. The top-layer thickness was 50 nm for both TWS and WTS samples, whereas the thickness of the bottom layer was $\sim$150 nm for sample TWS (WO_3 layer) and $\sim$200 nm for WTS (TiO_2 layer).

The film structure was determined by XRD, performed on a Shimadzu XRD–6000 diffractometer using Cu Kα radiation (λ = 1.5406 Å). Elemental composition and atomic concentration depth profile of the bilayer films were determined by the XPS technique, carried out on a Physical Electronics PHI-5000 VersaProbe spectrometer equipped with a monochromatic Al Kα radiation source (1486.6 eV). The energies in the XPS spectra were calibrated by using the C 1*s* level (284.6 eV) of the adventitious carbon as an internal reference. The concentration depth profiles were acquired by etching the sample surface with Ar^+ ions (1 keV, 500 nA beam current). XPS data processing was done using the PHI-MultiPak software.

Local structure around the metallic atoms was investigated by EXAFS spectroscopy at the Ti K (4966 eV) and W L_3 (10207 eV) edges. The primary absorption spectra (including the XANES and EXAFS ranges) were performed at the beamlines A1 (Ti K) and CEMO (W L_3) of the HASYLAB synchrotron-radiation facility (Hamburg, Germany). The incident radiation was analyzed by a Si(111) double-crystal monochromator and the absorption was measured in fluorescence mode. Powdered TiO_2 (anatase) and a WO_3 thin film were also measured, with a transmission setup for the former compound.

The EXAFS data were analyzed by a standard procedure, using the REX2000 package [20]. The pre-edge background was subtracted from the spectra, after its fit with a Victoreen formula. The EXAFS function $\chi(k)$ (where k is photoelectron wave number) was subsequently calculated from the absorption oscillations normalized through the atomic absorption (approximated by the smooth post-edge background). The $k^3\chi(k)$ spectra were Fourier transformed into physical r space resulting in radial atomic quasi-distributions with maxima corresponding, up to systematic shifts, to the neighboring shells of the absorbing atoms (Ti, W). The Fourier inversion of EXAFS was performed over the k-ranges 3.2–12.2 $Å^{-1}$ and

2.8–12.6 $Å^{-1}$ for the Ti K and W L_3 edges, respectively. The first three maxima of the Fourier transforms (FT) of the TiO_2-WO_3 films, corresponding to the O and Ti neighbors of the absorbing atoms, were isolated by Hanning windows and back-transformed into the *k* space. The so-filtered spectra, describing the EXAFS contribution of the selected neighboring shells, were non-linearly fitted with structural models, by a least-square method. The fit provided the structural parameters of the close surrounding of the absorbing atoms, i.e. the number (*N*) of the neighboring atoms, the absorbing atom−neighbor mean distances (*R*), and their mean square fluctuation (σ^2) around average values.

The EXAFS standards (electron backscattering amplitudes, phase-shifts, and mean free path between inelastic scatterings) characteristic of the Ti-O and Ti–Ti atomic pairs were derived from the spectrum of the anatase TiO_2, of known structure [21]. During the fit of the TiO_2 EXAFS, we have neglected the contribution of the higher oxygen neighbors (beyond 3.5 Å), superposed to the contribution of the titanium neighbors. This approximation is reasonable, taking into account that the oxygen contribution to EXAFS in the fitted *k* range is smaller than that of titanium by a factor of two to three. The EXAFS standards of the W-O and W-Ti pairs were calculated by the FEFF6 code [22]. The WO_3 film, of monoclinic structure [23], could not be used as a reference compound for the W-O distance, due to the split of the nearest oxygen shell around the W atoms. The *R*-factor of the fit of k^3-weighted EXAFS varied between 0.04 and 0.08.

10.3 Results and Discussion

10.3.1 XRD Analysis

The XRD patterns of the TWS and WTS bilayers (Fig. 10.1) show the (002), (020), and (200) maxima of the monoclinic WO_3 (JCPDS card no. 43-1035, space group $P2_1/n$), known to be the most stable phase of the bulk WO_3 at temperatures up to 330 °C [24]. However, the coexistence of this phase with a triclinic one (JCPDS card no. 32-1395) cannot be definitely ruled out, taking into account the close similarity of their diffraction patterns. The (002) and (020) maxima (at $2\theta = 23.1°$ and 23.6°, respectively) of these phases are superposed in the XRD patterns, due to their broadening by crystallite-size effects and instrumental resolution.

The TiO_2 layer is manifest by the (110) peak of the rutile structure (JCPDS card no. 21-1276), of a high intensity in the pattern of the sample WTS. This peak markedly diminishes in the TWS pattern, while the (101) peak of anatase (JCPDS card no. 21-1272) becomes visible, pointing out the presence of the both phases in this film. The Si substrate contributes to XRD plots by the Si (111) maximum, at $2\theta = 28.4°$.

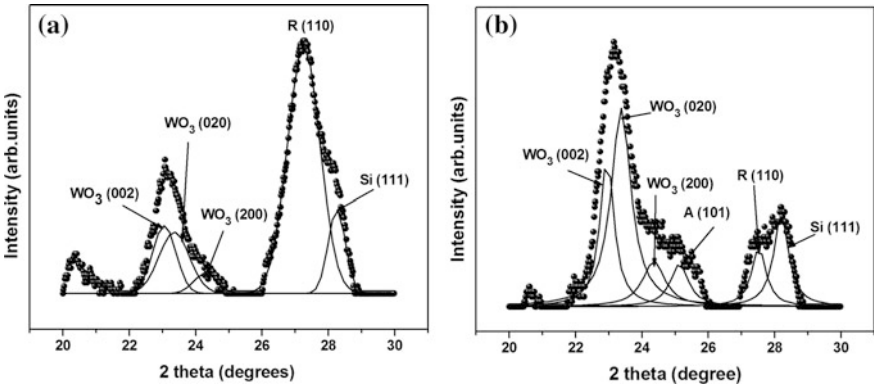

Fig. 10.1 Details of the diffraction patterns of the samples WTS (**a**) and TWS (**b**), including the most intense maxima of WO_3, rutile TiO_2 (R), and anatase TiO_2 (A)

10.3.2 XPS Analysis

The XPS survey spectrum of the WTS film (Fig. 10.2) displays the W core-level peaks of the WO_3 overlayer. A detail of the TWS spectrum was also shown on top of the figure, with the most intense Ti $2p_{3/2,1/2}$ peaks of the TiO_2 top layer. Both spectra show the XPS signals of the top layer exclusively, without a visible contribution from the bottom layer. This is due to the mean-free path λ of the photoelectrons, which is limited to about 15 Å for the measured kinetic energies of the photoelectrons. The corresponding escape depth, estimated as $\sim 3\ \lambda$, is smaller

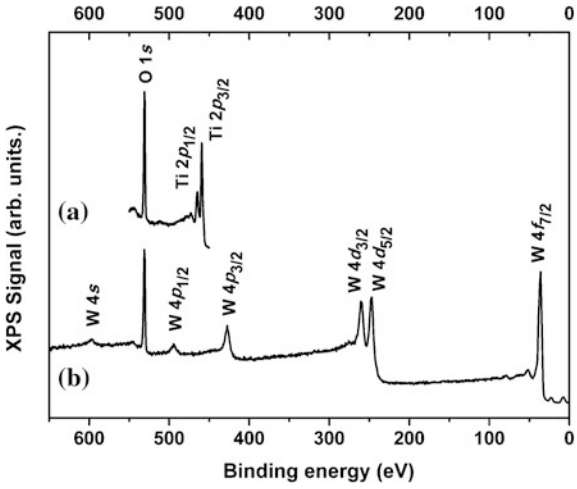

Fig. 10.2 XPS survey spectra of the TWS (**a**) and WTS (**b**) samples

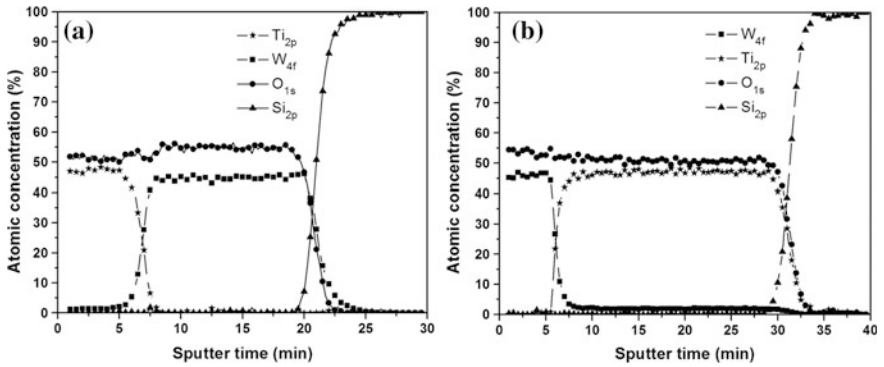

Fig. 10.3 The chemical depth profiles of samples TWS (**a**) and WTS (**b**)

than ∼45 Å, thus slightly inferior to the overlayer thickness. The elemental analysis of the film surface, carried out on narrow-scan spectra (not shown here), confirmed the WO_3 stoichiometry of the upper layer in the WTS sample.

The XPS depth profiles of the elemental composition of the TWS and WTS films are shown in Fig. 10.3. The quantitative analysis of the elemental concentration around the bilayer interface has been done taking into account the sensitivity factors of titanium and tungsten [25]. A sharp TiO_2-WO_3 interface is evidenced after etching the 50 nm thickness WO_3 (WTS) or TiO_2 (TWS) top layer by Ar^+ ion bombardment. After further removal of the bottom layer (TiO_2 in WTS and WO_3 in TWS), the next interface, with the Si substrate, became also clearly visible.

The XPS depth profiles of the two samples explain the intensity ratios between the XRD maxima of the TiO_2 and WO_3 layers. In WTS, the thin WO_3 overlayer contributes by weaker peaks with respect to the TiO_2 bottom layer, of a thickness about four times larger. By contrast, the WO_3 sublayer in TWS is thicker than the TiO_2 overlayer and its diffraction maxima are correspondingly stronger. As will be further discussed, a partial rutile-to-anatase transition takes place at the TiO_2-WO_3 interface, caused by the W inclusion into the TiO_2 lattice. The A(101) peak in the diffraction pattern of the sample TWS corresponds to the interface anatase. As shown by the XPS depth profile, the interface region in this sample is rather broad, of a thickness relatively comparable with that of the rutile TiO_2 overlayer. Consequently, both R(110) and A(101) peaks are visible in the XRD pattern, with comparable intensities. The interface is much narrower than the rutile sublayer in the sample WTS, which makes the A(101) peak hardly visible on the XRD pattern. The strongest peak of the WTS pattern is R(110), contributed by the dominating rutile sublayer.

10.3.3 Ti K-Edge XANES

The Ti K-edge XANES spectra (normalized to the absorption at ~280 eV above the edge) of the TiO_2-WO_3 films and anatase TiO_2 are shown in Fig. 10.4. The pre-edge (A_1–A_3) and edge (C_1–C_3) spectral features of the samples TWS and WTS are specific to the rutile structure [26–28]. The both pre-edge and edge features of the experimental XANES spectra of rutile and anatase were theoretically reproduced by band-structure and multiple-scattering calculations on atomic clusters sufficiently large around the absorbing Ti atom, connecting the atomic arrangements and electronic structures of the two titanium oxides with the positions and intensities of the spectral features [26, 27, 29]. Although the origin of the rutile XANES features was rather controversial in literature, the pre-edge peaks were generally explained by the mixture of the 3*d* and 4*p* orbitals of Ti atoms on the same or neighboring sites of the structure [26, 29–33]. Wu et al. [29] attributed the first and second pre-edge peaks (A_1, A_2) to dipolar transitions of the photoelectrons from Ti 1*s* to the 4*p* orbital of the absorbing Ti atom hybridized with 3*d* orbitals of the neighboring Ti atoms, split by the octahedral crystal field into t_{2g} and e_g band-like states. The A_3 peak was assigned by the same authors to the transitions on Ti 4*p* hybridized with the 4*s* orbitals of the neighboring Ti atoms and/or 2*p* orbitals of the O atoms. The C_1–C_3 crests were assigned to the transitions on Ti 4*p* states hybridized with O 2*p* states.

As shown by Fig. 10.4, the edge features C_1–C_3 are more sensitive to the changes of the local structure around Ti by going from anatase to rutile, resulting in more marked differences in this range with respect to the pre-edge peaks. The C_1–

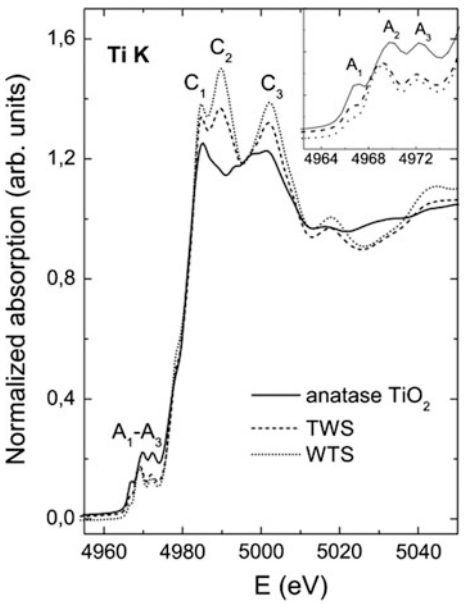

Fig. 10.4 Ti K-edge XANES normalized spectra of the TiO_2-WO_3 films and anatase TiO_2. The spectra were vertically translated for the sake of clarity. A detail with the pre-edge peaks of the spectra is shown in the inset

C_3 peaks undoubtedly point out the rutile structure of TiO_2 in the TiO_2-WO_3 films, in agreement with the XRD results. However, the reduced intensities of the C_2 and C_3 peaks of the sample TWS, somehow closer to the anatase XANES, could indicate a small TiO_2 fraction of anatase-like structure in this sample. This is also in line with the XRD pattern of the sample TWS, containing a faint anatase contribution (A(101) maximum in Fig. 10.1b).

10.3.4 EXAFS Measurements

10.3.4.1 Ti Environment

The k^3-weighted EXAFS of the Ti K and W L_3 edges, as well as the magnitude of the corresponding Fourier transforms (FT) are shown in Fig. 10.5, for the TiO_2-WO_3 bilayers and the anatase TiO_2 and WO_3 oxides. In the tetragonal structure of anatase TiO_2 [21], Ti is surrounded by six oxygen neighbors at a mean distance of 1.95 Å and by farther Ti neighbors at 3.04 Å (4 Ti1) and 3.78 Å (4 Ti2). The three main maxima of the anatase FT (Fig. 10.5b) correspond to this environment.

The rutile structure [34], despite the same tetragonal symmetry, shows several changes of the Ti environment. The oxygen surrounding is practically the same as in anatase, but the Ti neighbors arrange differently (see Table 10.1). The number of the Ti1 neighbors (N_{Ti1}) is reduced to a half (2 instead of 4 in anatase), whereas

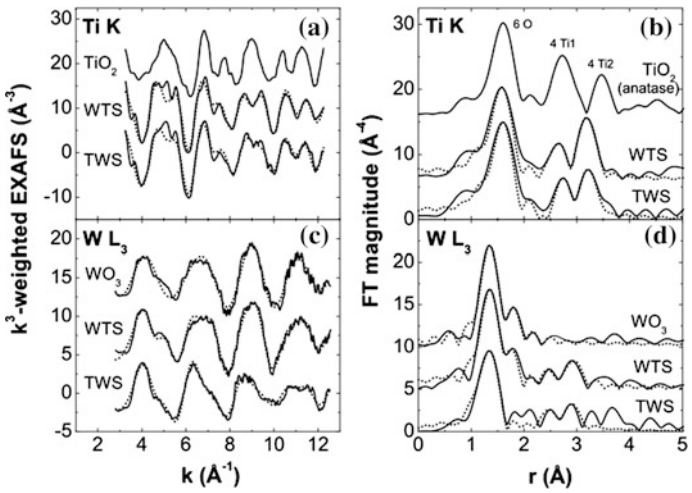

Fig. 10.5 **a**, **c** k^3-weighted EXAFS of the Ti K and W L_3 edges of the TiO_2-WO_3 bilayers, anatase TiO_2 and WO_3. **b**, **d** Magnitude of the corresponding Fourier transforms. The raw data and their fit with the O and Ti neighbors of the absorbing atoms were shown by continuous lines and dots, respectively. The EXAFS spectra and their transforms were vertically shifted for clarity

N_{Ti2} doubles to 8. The distances to the Ti1 and Ti2 neighbors also shorten with respect to the anatase structure, by about 0.10 and 0.20 Å, respectively. The shift towards smaller distances of the maxima corresponding to the Ti shells in the FTs of the samples TWS and WTS, more visible for the Ti2 neighbors, indicates the rutile structure of the TiO_2 layers in the TiO_2-WO_3 films. This result is in accord with the presence of the rutile (110) peak in the diffraction patterns of the samples. However, the weak anatase (101) peak in the XRD pattern of the sample TWS suggests a partial rutile-to-anatase transition of TiO_2 in this sample. A more detailed description of the Ti environment was possible by the fit of EXAFS. The results of the fit, i.e. coordination numbers (N) and interatomic distances (R), were given in Table 10.1. For simplification, the mean-square fluctuations (σ^2) of the interatomic distances, less relevant in the further analysis, were not indicated in the table.

The nearest surrounding of Ti in the TiO_2-WO_3 bilayers, consisting of six oxygen ions at 1.95 Å, closely resembles the rutile structure. However this is not very conclusive, since the Ti-O distance differs by only 0.01 Å in anatase and rutile, within the fit uncertainties. The next-nearest neighboring of Ti (Ti1 and Ti2 cations) in the sample WTS is characteristic of the rutile structure, although the depletion of the Ti2 neighbors, from $N_{Ti2} = 8$ in rutile to $N_{Ti2} = 4$ in WTS, suggests a defective structure, with Ti vacancies at larger distances.

A partial rutile-to-anatase transition is manifest for the sample TWS, with Ti2 neighbors at 3.56 Å, close to the rutile structure, but with 3 Ti1 at 3.04 Å, almost identical with the anatase structure. This environment points out a mixture of the initial rutile matrix and a developing anatase phase. The long-distance Ti2 neighbors in the anatase phase are probably strongly disordered, so that their contribution at around 3.78 Å wipes out of EXAFS.

10.3.4.2 W Environment

At the growth temperature (200 °C) of the WO_3 and TiO_2-WO_3 films, the WO_3 structure is expectedly monoclinic [24]. However, as previously observed for WO_3 thin films deposited under 300 °C, the presence of the both monoclinic and triclinic polymorphs in the WO_3 structure cannot be entirely precluded [35]. Despite their different symmetries, these varieties have closely related structures [23, 36], resulting in similar long-range order and diffraction patterns. The short-range order (W environment) is also almost identical in the two phases, as shown in Table 10.1. This makes quite difficult to distinguish between them by XRD or EXAFS. However, the possible presence of a triclinic phase in the WO_3 layers, besides the stable monoclinic form, does not change the further analysis focused on the TiO_2-WO_3 interface interaction.

The WO_3 structure generally consists of an arrangement of distorted corner-sharing WO_6 octahedra. The shape of these octahedra and the W-O distances depend on the particular symmetry of the WO_3 structure (triclinic, monoclinic, orthorhombic, tetragonal, or hexagonal). In the monoclinic structure, the W atoms are surrounded by four and two oxygen nearest-neighbors at 1.82 and 2.14 Å,

Table 10.1 Ti and W environments in the investigated samples compared to the reference titanium and tungsten oxides. The fit uncertainties on the last significant digit of the EXAFS-derived parameters are shown between parantheses

Sample	**Ti environment**		
TiO_2 rutile	6 O / 1.96 Å	2 Ti1 / 2.96 Å	8 O / 3.52 Å 8 Ti2 / 3.57 Å
TiO_2 anatase	6 O / 1.95 Å	4 Ti1 / 3.04 Å	4 Ti2 / 3.78 Å 8 O / 3.86 Å
WTS	6 (1) O / 1.95 (1) Å	2 (1) Ti1 / 2.96 (1) Å	4 (1) Ti2 / 3.543 (5) Å
TWS	6 (1) O / 1.95 (1) Å	3.0 (6) Ti1 / 3.04 (1) Å	1.9 (4) Ti2 / 3.562 (5) Å
Sample	**W environment**		
WO_3 monoclinic	4 O / 1.82 Å 2 O / 2.14 Å		4 W / 3.79 Å 6 O / 3.81 Å
WO_3 triclinic	4 O / 1.83 Å 2 O / 2.12 Å		3 W / 3.79 Å 6 O / 3.81 Å
WO_3 film	4 (1) O / 1.82 (1) Å 2 (2) O / 2.14 (3) Å		
WTS	4 (1) O / 1.81 (1) Å 2 (2) O / 2.13 (3) Å	1.4 (6) Ti1 / 2.96 (3) Å 1.6 (5) Ti1 / 3.14 (2) Å	
TWS	3.8 (5) O / 1.814 (6) Å	0.7 (4) Ti1 / 2.93 (3) Å 1.4 (4) Ti1 / 3.10 (2) Å	

respectively (see Table 10.1). The split main maximum of the EXAFS FT of the WO_3 film (Fig. 10.5d) describes this surrounding. A similar split is observed for the sample WTS, but it is absent for the sample TWS. This indicates a defective or disordered WO_3–like structure in the latter sample, with vacant or strongly disordered oxygen sites around W. The next-nearest neighbors (4 W and 6 O ions at the average distances 3.79 and 3.81 Å, respectively) do not significantly contribute to the FTs of EXAFS, also related to disordering effects.

The most interesting details in the Fourier transforms of the W L_3-edge EXAFS are the two faint maxima in the range 2.2–3.2 Å, susceptible to be attributed to Ti neighbors, similarly with the FTs of the Ti K-edge EXAFS. Such a neighborhood demonstrates the W incorporation into the TiO_2 lattice, on Ti sites, at the TiO_2-WO_3 interface. The first FT main maximum describes the W atoms in the WO_3 structure, while the next two maxima correspond to the fraction of W substituting for Ti in the TiO_2 lattice. The fit of the W-L_3 EXAFS (Table 10.1) points out the same nearest oxygen neighboring in the sample WTS as in the WO_3 film. The absence of the longer-distance O neighbors in TWS could suggest rather severe oxygen depletion around W. However, this result is intriguing, since it would imply the lack of the oxygen planes in the alternating O and WO_2 planes in the normal structure of WO_3. Such a change should have significant effects on the XRD pattern, which were not actually observed. More plausibly, the O neighbors at 2.14 Å still exist, but in a highly disordered arrangement. This weakens their contribution to EXAFS, under the level of statistical noise in the spectrum.

The W-Ti distances range in two narrow intervals: 2.93–2.96 Å, specific to the rutile TiO_2, and 3.10–3.14 Å, close to the anatase structure. This corresponds to two kinds of substitutional W insertion into the TiO_2 host: one with preserving the rutile structure of the host and the other with a change of the local surrounding towards the anatase symmetry. Therefore at interface, a fraction of the substitutional W brings about a transition of the rutile host towards anatase. The other W ions are accommodated on the Ti sites without altering the rutile symmetry of the host lattice.

It is worthwhile mentioning that the second and third maxima in the FTs of the Ti-K EXAFS describe the Ti1 and Ti2 neighboring shells, respectively, in the rutile or anatase structure, while these maxima in the FTs of the W-L_3 EXAFS corresponds to Ti1 shells only in the rutile and anatase-like environments. The Ti2 contribution is not seen in the latter FTs, probably due to their disordered arrangement. This contribution is clearly visible in the transforms of the Ti-K EXAFS since all Ti ions belong to the TiO_2 lattice, enhancing the Ti1,2 signals. In the case of the W-L_3 EXAFS, only a W fraction lies on Ti sites, which strongly diminishes the contribution of the Ti neighbors to EXAFS. An additional reduction of the Ti2 signal by disorder effects can thus easily eliminate it from FTs.

For the substitutional W in the rutile structure, the W-Ti1 distances are almost the same as the Ti-Ti1 distances in the rutile-TiO_2 host. This indicates the W incorporation in the rutile lattice as W^{6+} ions, of a similar radius with that of Ti^{4+} (W^{6+}: 0.60 Å; Ti^{4+}: 0.605 Å, for sixfold coordination [37]). This leaves the local rutile structure almost unmodified around W, but generates defects such as Ti^{4+} vacancies [38, 39] or Ti^{3+} ions [40, 41] to compensate the extra charge of the W^{6+} ions. On the contrary, for the W fraction with anatase-like environment, the W-Ti1 distance elongates by 0.06–0.10 Å with respect to the Ti-Ti1 distance in anatase. This suggests substitutional W^{4+} ions, of a larger radius (0.66 Å) than that of Ti^{4+}. In this case there is no charge imbalance between the dopant and host cations, but the more voluminous W^{4+} ions force the change of the local rutile surrounding towards an anatase structure and move away the Ti neighbors. Obviously, such an elongation effect should be manifest for the W-O distances too. However, it cannot be observed because the EXAFS signal of the W-O distances around substitutional W is dominated by that contributed by the W-O distances in the WO_3 majority phase

As shown by the above analysis, the TiO_2-WO_3 interface contributes to EXAFS in different ways for the Ti K and W L_3 edges, describing the Ti and W environments, respectively. The interface signature in the Ti environment consists of the partial rutile-to-anatase transition, induced by the substitutional W^{4+} ions. This is shown by the Ti-Ti1 distance of 3.04 Å, specific to anatase, in the TWS structure. In this sample, the TiO_2 overlayer has the thickness relatively comparable with that of the interface (see Fig. 10.3a), and both 'bulk' rutile and interface anatase contribute to EXAFS. This is similar with the superposed contributions of the two phases to the XRD pattern of the sample TWS (see Fig. 10.1b). In the case of the sample WTS, the EXAFS signal of the bulky rutile sublayer (see Fig. 10.3b) dominates the interface signal, i.e. the anatase contribution, and both Ti-Ti1 and Ti-Ti2 distances are specific to the rutile structure.

The interface contribution to the W environment consists of the Ti neighboring of the W ions incorporated in the TiO_2 lattice. The W-Ti distances are specific to the rutile and anatase lattices, corresponding to the substitutional W^{6+} and W^{4+} ions, respectively. The W L_3-edge EXAFS 'feels' the interface regardless of its relative thickness with respect to that of the WO_3 layer. This is so because the contributions of the interface (W-Ti distances) and WO_3 layer (W-O distances) are well separated in the Fourier transforms of EXAFS.

10.3.5 XPS Analysis of the Interface

While the +6 oxidation state of substitutional W in W-doped TiO_2 is currently accepted, the presence of substitutional W^{4+} ions was seldom reported [42]. In order to verify the formation of these ions at the TiO_2-WO_3 interface, we measured the W 4*f* XPS spectrum of the WTS and TWS samples, after their Ar etching, with sputtering times corresponding to the interface (see Fig. 10.3).

Unfortunately, the Ar^+ bombardment has a reducing effect on the W and Ti ions, preventing a correct determination of the W oxidation states. This is clearly seen in Fig. 10.6, illustrating the W 4*f* spectrum of the sample WTS at increasing sputtering times. For the uppermost WO_3 layers, with no Ar sputtering, the $4f_{7/2,5/2}$ doublet is well resolved, with peaks at 35.7 and 37.9 eV, specific to the W^{6+} ions in WO_3 [43]. After a sputtering of 15 s, exposing the subsurface WO_3 layers, the doublet displays a marked broadening due to additional contributions at 33.2 and 35.4 eV, characteristic of the W^{4+} state [44]. Obviously, the partial reduction of W^{6+} to W^{4+} in this region, much closer to the surface than to the WO_3-TiO_2 interface, is an effect of the Ar sputtering. Moreover, similar reduction effects of the ion bombardment were earlier reported for TiO_2 thin films, with changes of TiO_2 to Ti_2O_3 or TiO, depending on the sputtering time [45, 46].

In the WO_3-TiO_2 films, W can even reach the metallic state, for long enough sputtering times. This is the case of the WO_3-TiO_2 interface, accessed by XPS after 6.5 min of Ar sputtering (Fig. 10.6c). The W 4*f* spectrum of the interface exhibits, besides the W^{6+} and W^{4+} contributions, two sharp peaks at 31.3 and 33.5 eV, corresponding to the $4f_{7/2,5/2}$ doublet of metallic W [47]. The W^0 $5p_{3/2}$ and W^{4+} $5p_{3/2}$ peaks are visible as well at 37.2 and 39.3 eV, respectively. Ti is also partially reduced to the metallic state, as pointed out by the faint Ti^0 $3p_{3/2}$ peak at 32.2 eV [48]. Other contributions of the Ti states (3+, 4+) to the spectrum are difficult to be unambiguously established, since they superpose over the W peaks: the Ti^{3+} $3p_{3/2}$ peak at 36.0 eV [49] superposes over W^{6+} $4f_{7/2}$, while Ti^{4+} $3p_{3/2}$ at 37.3 eV [50] has practically same binding energy as W^0 $5p_{3/2}$.

Due to the large number of components contributing to the interface spectrum, its fitting analysis is not beyond any doubt, making rather uncertain the relative weights of the different W and Ti states. However, the presence of intense W^0 $4f_{7/2,5/2}$ peaks clearly demonstrates the W reduction to the metallic state after a long sputtering time, corresponding to the WO_3-TiO_2 interface. These results show that

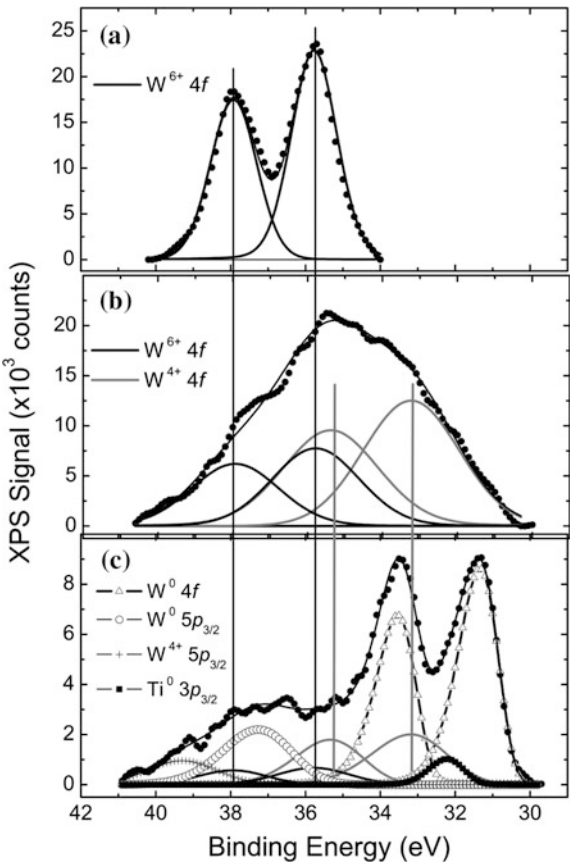

Fig. 10.6 W 4*f* core-level XPS spectra of: **a** uppermost WO_3 layer of the sample WTS, without Ar sputtering; **b** subsurface WO_3 layer, after Ar sputtering of 15 s; **c** WO_3-TiO_2 interface, after Ar sputtering of 6.5 min. The positions of the W^{6+} and W^{4+} $4f_{7/2,5/2}$ peaks are indicated by vertical guidelines

the XPS determination of the W states (and implicitly the confirmation of the W^{4+} species) at the interface cannot give reliable results, due to the chemical changes caused by the Ar^+ bombardment.

10.4 Conclusions

TiO_2/WO_3 and WO_3/TiO_2 bilayer structures have been grown on Si single-crystal substrates by PVD. Combined XRD, XPS, XANES, and EXAFS analyses evidenced the W substitution for Ti in the TiO_2 lattice at the TiO_2-WO_3 interface. A fraction of the substitutional W enters the TiO_2 lattice as W^{6+} ions, leaving almost unchanged the rutile structure of the host matrix. The other fraction, consisting of W^{4+} ions, changes the local surrounding towards the anatase symmetry. The substituting W^{4+} ions also cause a local expansion of the anatase lattice, due to the difference between the ionic radii of W^{4+} (0.66 Å) and Ti^{4+} (0.60). These results

highlight specific interface phenomena in TiO_2-based composite semiconductors, with expected effects on their photocatalytic properties and of relevance for further implementation in environmental and energy-related applications.

Acknowledgements Two of the authors (DM and CMT) have contributed to this work within the "Kernel" Project PN09-450101, funded by the Romanian Ministry of Education and the National Authority for Scientific Research. Part of the investigations have been done in the frame the COFOBIST project financed by the Romanian Ministry of Education (proj. 697/2013).

References

1. M.R. Hoffmann, S.T. Martin, W. Choi, D.W. Bahnemann, Chem. Rev. **95**, 69 (1995)
2. Y. Cui, H. Du, L. Wen, J. Mater. Sci. Technol. **24**, 675 (2008)
3. M.I. Litter, J.A. Navío, J. Photochem. Photobiol., A **98**, 171 (1996)
4. J. Zhu, F. Chen, J. Zhang, H. Chen, M. Anpo, J. Photochem. Photobiol., A **180**, 196 (2006)
5. M.M. Mohamed, M.M. Al-Esaimi, J. Mol, Catal. A **255**, 53 (2006)
6. M. Takeuchi, H. Yamashita, M. Matsuoka, M. Anpo, T. Hirao, N. Itoh, N. Iwamoto, Catal. Lett. **67**, 135 (2000)
7. W. Li, A.I. Frenkel, J.C. Woicik, C.Ni, S. Ismat Shah, Phys. Rev. B **72**(155315), 1–6 (2005)
8. L. Diamandescu, F. Vasiliu, D. Tarabasanu-Mihaila, M. Feder, A.M. Vlaicu, C.M. Teodorescu, D. Macovei, I. Enculescu, V. Parvulescu, E. Mater, Chem. Phys. **112**, 146 (2008)
9. S. Matsuo, N. Sakaguchi, K. Yamada, T. Matsuo, H. Wakita, Appl. Surf. Sci. **228**, 233 (2004)
10. F.B. Li, X.Z. Li, M.F. Hou, Appl. Catal. B **48**, 185 (2004)
11. R. Asahi, T. Morikawa, T. Ohwaki, T. Aoki, I. Taga, Science **293**, 269 (2001)
12. A.V. Emeline, V.N. Kuznetsov, V.K. Rybchuk, N. Serpone, Int. J. Photoenergy **258394**, 1–19 (2008)
13. S.U.M. Khan, M. Al-Shahry, M.W.B. Ingler Jr, Science **297**, 2243 (2002)
14. J.C. Yu, J. Yu, W. Ho, Z. Jiang, L. Zhang, Chem. Mater. **14**,3808 (2002)
15. T. Ohno, M. Akiyoshi, T. Umebayashi, K. Asai, T. Mitsui, M. Matsumura, Appl. Catal. A **265**, 115 (2004)
16. L. Lin, W. Lin, Y. Zhu, B. Zhao, Y. Xie, Chem. Lett. **34**, 284 (2005)
17. O. Lorret, D. Francová, G. Waldner, N. Stelzer, Appl. Catal. B **91**, 39 (2009)
18. M. Miyauchi, A. Nakajima, K. Hashimoto, T. Watanabe, Adv. Mater. **12**, 1923 (2000)
19. D. Luca, D. Mardare, F. Iacomi, C.M. Teodorescu, Appl. Surf. Sci. **252**, 6122 (2006)
20. T. Taguchi, T. Ozawa, H. Yashiro, Phys. Scripta T **115**, 205 (2005)
21. C.J. Howard, T.M. Sabine, F. Dickson, Acta Crystallogr. B **47**, 462 (1991)
22. J.J. Rehr, J. Mustre de Leon, S.I. Zabinsky, R.C. Albers, J. Am. Chem. Soc. **113**, 5135 (1991); J. Mustre de Leon, J.J. Rehr, S.I. Zabinsky, R.C. Albers, Phys. Rev. B **44**, 4146 (1991)
23. P.M. Woodward, A.W. Sleight, T. Vogt, J. Phys. Chem. Solids **56**, 1305 (1995)
24. T. Vogt, P.M. Woodward, P.A. Hunter, J. Solid State Chem. **144**, 209 (1999); E. Cazzanelli, C. Vinegoni, G. Mariotto, A. Kuzmin, J. Purans, J. Solid State Chem. **143**, 24 (1999)
25. J.F. Moulder, W.F. Stickle, P.E. Sobol, K.D. Bomben, *Handbook of X-ray Photoelectron Spectrosopy* (Physical Electronics, USA, ULVAC-PHI Japan, 1995), p. 184
26. M.F. Ruiz-López, A. Muñoz-Pàez, J. Phys.: Condens. Matter **3**, 8981 (1991)
27. F. Farges, G.E. Brown Jr, J.J. Rehr, Phys. Rev. B **56**, 1809 (1997)
28. A. Niltharach, S. Kityakarn, A. Worayingyong, J.T- Thienprasert, W. Klysubun, P. Songsiriritthigul, S. Limpijumnong. Phys. B **407**, 2915 (2012)
29. Z.I. Wu, G. Ouvrard, P. Gressier, C.R. Natoli, Phys. Rev. B **55**, 10382 (1997)
30. B. Poumellec, J.F. Marucco, B. Touzelin, Phys. Rev. B **35**, 2284 (1987)
31. B. Poumellec, P.J. Durham, G.Y. Guo, J. Phys.: Condens. Matter **3**, 8195 (1991)

32. M.A. Khan, A. Kotani, J.-C. Parlebas, J. Phys.: Condens. Matter **3**, 1763 (1991)
33. T. Uozumi, K. Okada, A. Kotani, O. Durmeyer, J.P. Kappler, E. Beaurepaire, J.C. Parlebas, Europhys. Lett. **18**, 85 (1992)
34. K. Sugiyama, Y. Takeuchi, Z. Kristallogr. **194**, 305 (1991)
35. C.V. Ramana, S. Utsunomiya, R.C. Ewing, C.M. Julien, U. Becker, J. Phys. Chem. B **110**, 10430 (2006)
36. B.O. Loopstra, H.M. Rietveld, Acta Crystallogr. B **25**, 1420 (1969)
37. R.D. Shannon, Acta Crystallogr. **32**, 751 (1976)
38. A. Kubacka, G. Colon, M. Fernandez-Garcia, Catal. Today **143**, 286 (2009)
39. A.M. Márquez, J.J. Plata, Y. Ortega, J.F. Sanz, J. Phys. Chem. C **115**, 16970 (2011)
40. Y.C. Lee, Y.P. Hong, H.Y. Lee, H. Kim, Y.J. Jung, K.H. Ko, H.S. Jung, K.S. Hong, J. Colloid Interf. Sci. **267**, 127 (2003); K.H. Ko, Y.C. Lee, Y.J. Jung, J. Colloid Interf. Sci. **283**, 482 (2005)
41. E.S. Lee, Trans. Electr. Electron. Mater. **12**, 68 (2011)
42. D.M. Chen, G. Xu, L. Miao, L.H. Chen, S. Nakao, P. Jin, J. Appl. Phys. **107**, 063707–4 (2010)
43. A. Katrib, F. Hemming, P. Wehrer, L. Hilaire, G. Maire, J. Electron Spectrosc. Relat. Phenom. **76**, 195 (1995)
44. P.G. Gassman, D.W. Macomber, S.M. Willging, J. Am. Chem. Soc. **107**, 2380 (1985)
45. S. Hashimoto, A. Tanaka, A. Murata, T. Sakurada, Surf. Sci. **556**, 22 (2004)
46. D. Luca, D. Macovei, C.M. Teodorescu, Surf. Sci. **600**, 4342 (2006)
47. C.J. Powell, J. Electron Spectrosc. Relat. Phenom. **185**, 1–3 (2012)
48. A. Lebugle, U. Axelsson, R. Nyholm, N. Martensson, Phys. Scr. **23**, 825 (1981)
49. F. Werfel, O. Brummer, Phys. Scr. **28**, 92 (1983)
50. F. Lange, H. Schmelz, H. Knozinger, J. Electron Spectrosc. Relat. Phenom. **57**, 307 (1991)